Stress field in the source region after the 2007 M_w 6.6 Niigataken Chuetsu-oki earthquake deduced from aftershock focal mechanisms: Implication for a pre-mainshock stress field

Kazutoshi Imanishi and Yasuto Kuwahara

Geological Survey of Japan, AIST, AIST Tsukuba Central 7, 1-1-1, Higashi, Tsukuba, Ibaraki 305-8567, Japan

Stress fields in the source region before and after the 2007 M_w 6.6 Niigataken Chuetsu-oki earthquake were investigated using aftershock focal mechanism solutions. We have attempted to determine aftershock focal mechanisms using P-wave polarity data as well as body wave amplitudes because this earthquake occurred offshore, where observation station coverage is poor. This approach enabled us to obtain 76 well-determined aftershock focal mechanisms. Although the stress field in the studied area is known to be generally characterized by a reverse-faulting regime, the application of a stress tensor inversion method to the aftershock focal mechanisms revealed that the stress field spatially varied on a scale smaller than the fault dimension of the mainshock, with a mixture of strike-slip and reverse faulting regimes. The post-mainshock stress field estimated by the stress tensor inversion was compared with the theoretical stress field computed using an observed non-uniform slip distribution of the mainshock and variously assumed pre-shock stress fields. The results of this comparison suggest that the pre-mainshock principal stress in the WNW-ESE direction was dominant and that the magnitudes of the other two principal stresses were similar.
Key words: Niigataken Chuetsu-oki earthquake, aftershock focal mechanisms, pre-shock stress field, stress tensor inversion.

1. Introduction

The 2007 M_w 6.6 Niigataken Chuetsu-oki earthquake occurred on July 16, 2007, near the west coast of Niigata prefecture, Japan. The largest aftershock (M_w 5.7), which took place about 7 h after the mainshock, was located about 5 km southeast of the mainshock hypocenter. The focal mechanisms of the mainshock and the largest aftershock were reported by several institutes (e.g., Japan Meteorological Agency, Harvard University, and U.S. Geological Survey) and described as a pure reverse faulting with a strike in the NNE-SSW direction. The relocated aftershocks suggest that aftershocks were mainly distributed along the southeast dipping planes and that a northwest dipping plane might also exist near the hypocenter of the mainshock (Kato *et al.*, 2008; Yukutake *et al.*, 2008).

In 2004, an earthquake of M_w 6.6 occurred in the Niigata prefecture (2004 Mid-Niigata earthquake) (e.g., Kato *et al.*, 2006; Sibson, 2007), 40 km to the southeast of the 2007 earthquake. The following year, two magnitude-5-class earthquakes occurred between the source areas of the 2004 and the 2007 events. Hashimoto (1990), based on his analyses of triangulation data compiled over the past 100 years, detected a zone with high strain rates from Niigata to the Kinki district. This zone with high strain rates was also clearly identified in the recent observation of dense GPS ar-

rays by the Geographical Survey Institute and subsequently named the Niigata-Kobe Tectonic Zone (NKTZ) (Sagiya *et al.*, 2000) (Fig. 1). The strain rate in the NKTZ was determined to exceed 10^{-7}/year, which is tenfold higher than the average in Japan (Sagiya *et al.*, 2000; Mazzotti *et al.*, 2001). There are many active faults within this zone, and a number of historic large earthquakes have also occurred there (e.g., the 1995 M_w 6.9 Kobe earthquake), including both the 2007 and 2004 earthquakes. The occurrences of these earthquakes and their numerous aftershocks provide new insights on seismotectonics in this region. In particular, studies on aftershock focal mechanisms provide information on stress fields at seismogenic depths and reveal several aspects of the faulting that could not be inferred from the aftershock locations alone. For example, the pre-mainshock stress magnitude can be constrained by combining the focal mechanisms of aftershocks and/or background seismicity with the stress change due to the mainshock (e.g., Hardebeck and Hauksson, 2001; Wesson and Boyd, 2007; Yukutake *et al.*, 2007), which will provide a clue toward a better understanding of large earthquake occurrence.

Here, we first relocate the aftershocks of the 2007 Niigataken Chuetsu-oki earthquake based on appropriate velocity models in this region. We then determine aftershock focal mechanisms using P-wave polarity data as well as body wave amplitudes, which enables us to constrain the mechanisms of small earthquakes using the land seismic networks alone. A stress tensor inversion method is then applied to infer the stress field in the source region after the mainshock. Finally, the stress field is compared with
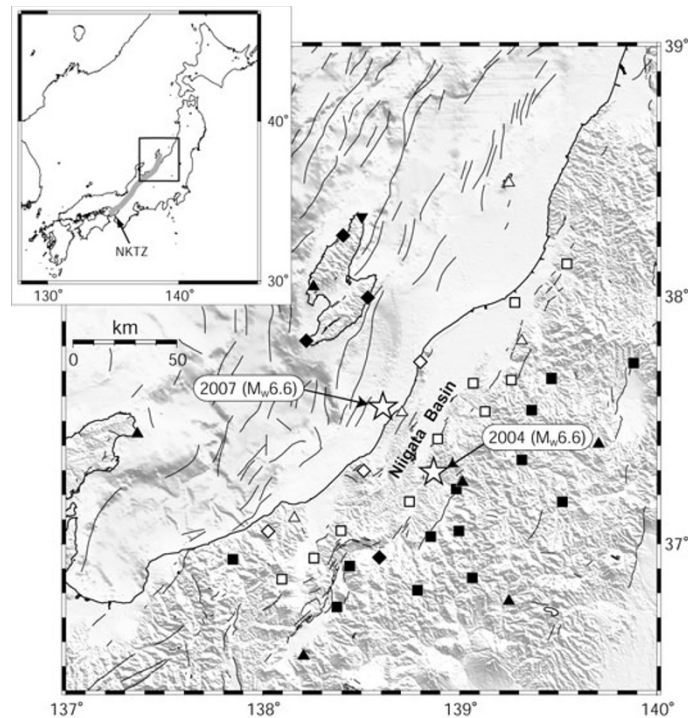
Fig. 1.   Distribution of the stations used for the relocation and the focal mechanism determinations. Permanent stations operated by NIED, JMA, ERI, and Tohoku University are represented by squares, triangles, diamonds, and reverse-triangles. Solid symbols are stations that were assigned the high-velocity model, and open symbols are stations assigned the low-velocity model in Fig. 2. Solid lines represent active faults (Research Group for Active Faults of Japan, 1991). Stars are the epicenters of the 2007 Niigataken Chuetsu-oki (M_w 6.6) and the 2004 Mid-Niigata earthquake (M_w 6.6). The thick gray line in the upper left inset shows the concentrated deformation zone (NKTZ).

the theoretically computed post-mainshock one to infer the pre-mainshock stress field.

2.   Data

Figure 1 shows the distributions of the permanent stations used in our study; these are operated by NIED (National Research Institute for Earth Science and Disaster Prevention), JMA (Japan Meteorological Agency), ERI (Earthquake Research Institute, Tokyo University), and Tohoku University. Each station is equipped with a set of three-component velocity transducers having a natural frequency of 1 or 2 Hz. Seismometers deployed by NIED (Hi-net) are installed at the bottom of a borehole at a depth of a few hundred meters (Okada *et al.*, 2004). Based on the JMA earthquake catalogue, we selected 1,933 aftershocks that occurred during the period from the occurrence of the 2007 earthquake to July 29, 2007. In order to compare the distribution of regional seismicity prior to the 2007 earthquake with that of the aftershock sequence, we also included 932 prior events since October 2001, which is when the Hi-net stations were installed, and the station distribution became almost the same as that depicted in Fig. 1.

3.   Hypocenter Locations

A refraction profile (Takeda *et al.*, 2004), geology (Yanagisawa *et al.*, 1985), the Bouguer gravity anomaly (Geological Survey of Japan, AIST, 2004), and tomographic imaging (Kato *et al.*, 2006) suggest that the Niigata basin is covered with thick sediments of Neogene and Quaternary and that there is a strong lateral variation of velocity
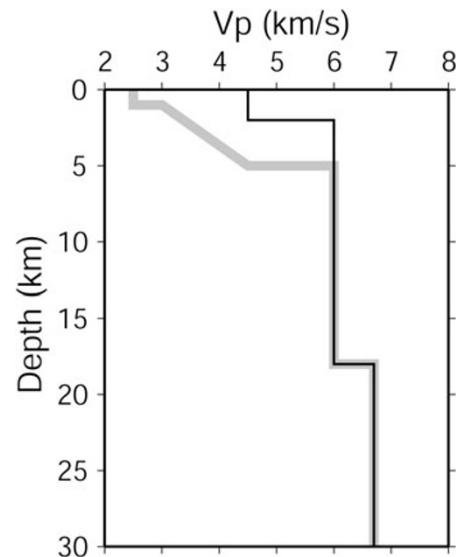

Fig. 2.   *P*-wave velocity structure models used for hypocenter determination. In the calculation of travel time, the velocity model shown by a black (gray) line is used for stations with solid (open) symbols in Fig. 1.

structure in the study area. We therefore assumed two different one-dimensional (1-D) crustal velocity structures for stations located around the Niigata basin and another region, respectively. The *P*-wave velocity model used in our investigation is also shown in Fig. 2, where the model for the stations around the Niigata basin has a lower velocity than that for the other stations at depths of less than 5 km.
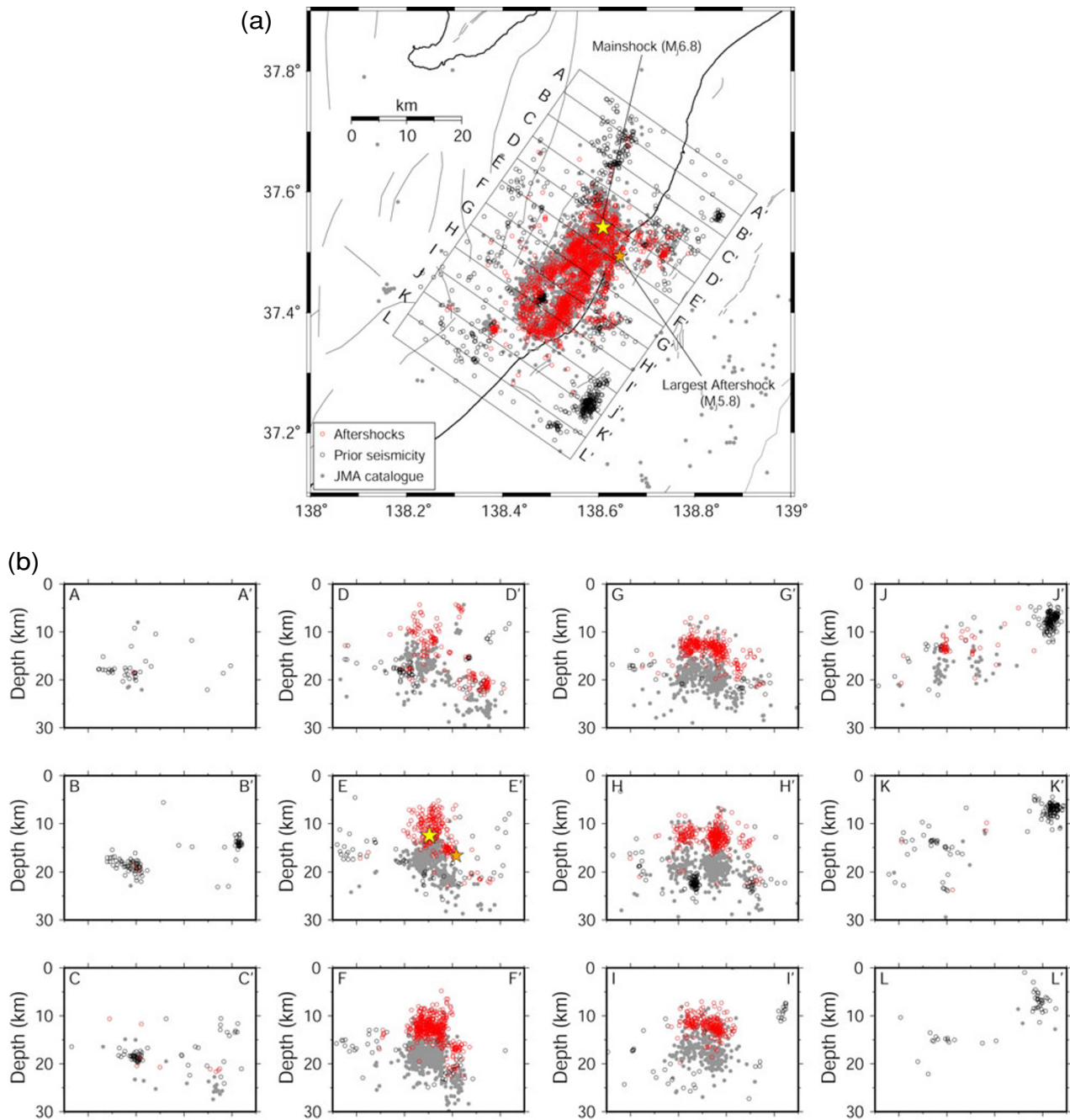
Fig. 3. Hypocenter locations determined in the present study. Prior seismicity (October 4, 2001 to July 14, 2007) and aftershocks (July 16 to July 29, 2007) are shown by black and red circles. Gray-filled circles show the locations determined by JMA during the period from July 16 to July 29, 2007. (a) Map view. (b) Vertical cross sections. Locations of each section are shown by rectangles in (a).

The S-wave models are assumed by scaling the P-wave velocities by a factor $1/\sqrt{3}$.

Using these two different velocity models and arrival time readings by JMA, the hypocenters were determined by a maximum-likelihood estimation algorithm (Hirata and Matsu'ura, 1987). We first determined all aftershocks without station-corrections. These aftershocks were then relocated by introducing the station correction, which was obtained using the average of the differences between observed and theoretical travel times at each station. We repeated the above procedure three times and obtained final locations as well as station-corrections at individual stations. The root mean squares (RMS) of the residuals de-

creased from 0.32 to 0.16 s for the P-wave and 0.61 to 0.28 s for the S-wave. The hypocenters of prior events were also determined using the same velocity structures and the station corrections.

Figure 3 shows the well-located events in map view and cross sections (red and black circles for aftershocks and prior events). Only events with small spatial errors of less than 1 km in the horizontal direction and 2 km in depth are plotted, where 1,823 aftershocks (94% of total aftershocks) and 862 prior events (92% of total events) are included. In map view (Fig. 3(a)), the aftershocks extend for 30 km in the NNE-SSW direction, and the zone is 15 km wide. The NNE-SSW direction agrees with the strikes of the nodal

planes of the mainshock focal mechanism as well as the general trend of active faults and folds in the surrounding area (Fig. 1). The epicenter of the mainshock locates around the northeast edge of this distribution, suggesting that the mainshock ruptured to the southwest unilaterally. Viewing the aftershock locations in cross sections (Fig. 3(b)), we found that the aftershocks distributed at depths from about 5 to 25 km and that most were located in a depth range of 5–15 km, indicating that the fault rupture did not reach the Earth's surface. It should be noted that most of prior seismicity occurred outside of the aftershock area and did not overlap with aftershock distributions. This may suggest that the background seismicity alone cannot illuminate individual or distinctive fault structures associated with the mainshock.

Compared with the distribution of the JMA catalogue (gray-filled circles in Fig. 3), the relocated aftershocks clustered and became shallower at about 5–10 km. The difference is primarily caused by the different velocity structures employed, since a strong lateral variation in velocity structure is not considered in the JMA earthquake catalogue.

The aftershocks in the northern region (D–D′ and E–E′ in Fig. 3) were widely dispersed with a depth range of 5–15 km, in which the mainshock was located at the bottom of the distribution (13 km). The focal mechanism of the mainshock is reverse faulting, but we cannot delineate a distinct fault plane associated with the mainshock. It should be noted that aftershocks in the southern region (G–G′, H–H′, and I–I′ in Fig. 3) show a feature that is different from any found in the aftershocks of northern region: the former cluster at 10–15 km and show a southeast dipping low-angle distribution with a dip of about 20° or less. There is a small aftershock zone in the middle of the southern region, which seems to be related with the area of large slip during the mainshock. The aftershocks were most active in the central region (F–F′ in Fig. 3), where hypocenters show a diffuse spatial pattern. It would appear that this region is a transition zone between the northern and southern regions. Aftershocks associated with the largest aftershock were distributed at a depth range of about 15–18 km and had a width of approximately 5 km (E–E′ and F–F′ in Fig. 3), which probably represents the fault plane of the largest aftershock. The epicenter of the largest aftershock is located at the northeast edge of this distribution, suggesting that the largest aftershock also ruptured to the southwest unilaterally. The cross-section of the E–E′ plane shows a southeast dipping plane with a dip angle of about 40°, which agrees with the focal mechanism solution of the largest aftershock. The depth range of these aftershocks was deeper than that of those in the northern, central, and southern regions. Several clusters occurred at a depth of 20–25 km, where background seismic activity was also present.

Yukutake *et al.* (2008) estimated aftershock distributions of the 2007 earthquake by applying a double-difference method (Waldhauser and Ellsworth, 2000) to both manually picked and waveform cross-correlation data which were observed at permanent online stations. Kato *et al.* (2008) determined the velocity structure and aftershock distributions of the 2007 earthquake by applying a double-difference tomography method (Zhang and Thurber, 2003) to arrival

times observed by a dense seismic network deployed immediately after the mainshock. The aftershock distributions determined in the above two studies present a sharper image than we obtained in our present study and reveal several discrete fault segments. In particular, the former two groups of researchers found that aftershocks in the northern region were distributed along both the northwestward- and southeastward-dipping planes. Furthermore, Kato *et al.* (2008) revealed a complex aftershock distribution with numerous conjugated fault planes in the central aftershock region, which corresponds to the F–F′ cross-section in Fig. 3.

Due to the insufficient number of stations above the aftershock area, there is a possibility that hypocenters determined in our study as well as those determined by Yukutake *et al.* (2008) and Kato *et al.* (2008) contain a large estimation error, especially in terms of event depths. Shinohara *et al.* (2008) determined the precise aftershock distribution using an ocean bottom seismometer network as well as a temporally installed and permanent on-land seismic network. The general features of their distribution, such as geometry and the depth range, are similar to those in our study. We believe that accuracy of our results with respect to aftershock locations is sufficient for the purpose of our study.

4. Focal Mechanism Solution of Aftershocks Using Body Wave Amplitudes

We determined focal mechanism solutions of aftershocks using absolute *P*- and *SH*-wave amplitudes as well as *P*-wave polarity. The same approach was used in Imanishi *et al.* (2006a, b, c) and shown to be effective for small earthquakes even if the number of *P*-wave polarities is insufficient and the observation station coverage is poor.

We analyzed aftershocks with M_j larger than 3 and at least ten *P*-wave polarities. Here, M_j is a magnitude determined by JMA. After correcting the instrumental response, we determined the spectral levels and corner frequencies of the spectra by fitting the ω^2-model (Boatwright, 1978) with an attenuation correction. The spectral levels for lower frequencies were used as observed amplitudes. Theoretical amplitudes were calculated from the far-field solutions for a shear point-source dislocation in a homogeneous infinite medium with corrections of the incident angles at the surface and geometrical spreading. The best-fit solution of each event was determined by minimizing the residual between the observed and theoretical amplitudes, where a grid search approach was conducted for strike, dip, and slip angles at 5°-intervals. Since amplitudes are used, the seismic moment of each event can also be determined. We then calculated the logarithmic average of the ratios between the theoretical and observed amplitudes of all analyzed events and used this average as the amplitude station correction at each station. Using these amplitude station corrections, we then redetermined focal mechanism solutions and seismic moments. The stability of the solution was checked by plotting all focal mechanisms whose residual is less than 1.1-fold the minimum residual value. We rejected ambiguous solutions where multiple solutions were possible. In total, we selected 76 focal mechanisms. During the same period, the numbers of routinely determined first-motion focal mechanisms by JMA and moment tensor solutions by NIED
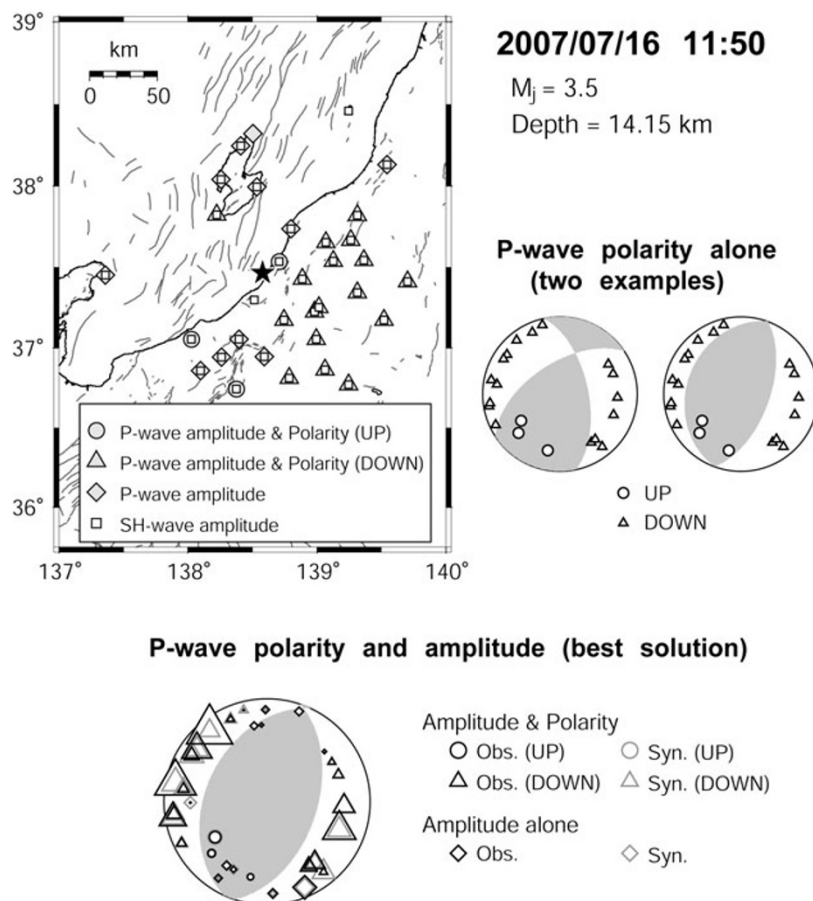
Fig. 4. An example of focal mechanism determination for an earthquake (M_j 3.5) that occurred at 11:50 JST on July 16, 2007. A map of the epicenter (solid star) and station distribution are shown in the upper left. A unique focal mechanism solution cannot be determined using P-wave polarity data alone (upper right), while it is possible to determine a unique solution (pure reverse faulting) using absolute P and SH amplitudes and P-wave polarity (bottom). Focal mechanism solutions are projected onto the lower hemisphere using the equal-area projection, where circles and triangles denote compressional and dilatational first motions, respectively. The sizes of each symbol are proportional to logarithmic amplitudes, respectively.

were 24 and 15, respectively.

Figure 4 shows an example of focal mechanism determination for an earthquake (M_j 3.5) that occurred at 11:50 JST on July 16, 2007. As is evident from this figure, P-wave first-motion polarity alone cannot constrain the mechanism of this earthquake. In addition to a pure reverse faulting-type mechanism, a reverse faulting with a strike-slip component also perfectly explains the first motion P-wave polarities. On the other hand, absolute amplitudes and the polarity observation require the pure reverse faulting-type mechanism. All of the single-event focal mechanism solutions determined in our study are shown in Fig. 5 together with the first-motion polarities. The estimated solutions explain the first-motion polarities well. The focal mechanisms are plotted on maps in Fig. 6, where different colors are used to differentiate reverse (green), strike-slip (red), and normal (blue) faulting mechanisms. For the mainshock and largest aftershock, we plotted the P-wave first-motion solutions determined by JMA. Following Flohlich (1992), we classified reverse events as those having T-axis plunges of less than 40° and strike-slip and normal fault earthquakes as those having B- and P-axis plunges of less than 30°, respectively. All remaining events were defined as 'other'. The number of reverse, strike-slip, normal, and other events are 35, 10, 6, and 25, respectively. A triangle diagram is shown

in the inset of Fig. 6(a), which suggests that half of the other events are a mixture of reverse and strike-slip components. A diversity of aftershock focal mechanisms were present, as is evident from the numerous well-documented examples, such as the 1989 M_w 6.9 Loma Prieta (Zoback and Beroza, 1993), the 1994 M_w 6.8 Northridge (Hauksson et al., 1995), and the 2004 M_w 6.6 Mid Niigata prefecture (Kato et al., 2006) earthquakes. It should be noted that many aftershocks with large strike-slip components occurred across the entire region and that a high diversity of aftershock focal mechanisms seemed to be particularly concentrated in the central region.

5. Stress Field in the Source Region After the Mainshock

Using the focal mechanism solutions determined in our study, we calculated the stress field in the aftershock region by applying the inversion method of Michael (1984). The inversion solves the orientation of the three principal stress axes and the relative magnitude of the principal stresses defined by $\phi = (S_2 - S_3)/(S_1 - S_3)$, where S_1, S_2, and S_3 are the maximum, intermediate, and minimum compressive principal stresses, respectively. Since the stress tensor inversion method assumes that all of the earthquakes included in the inversion occur under a single stress state, we divided
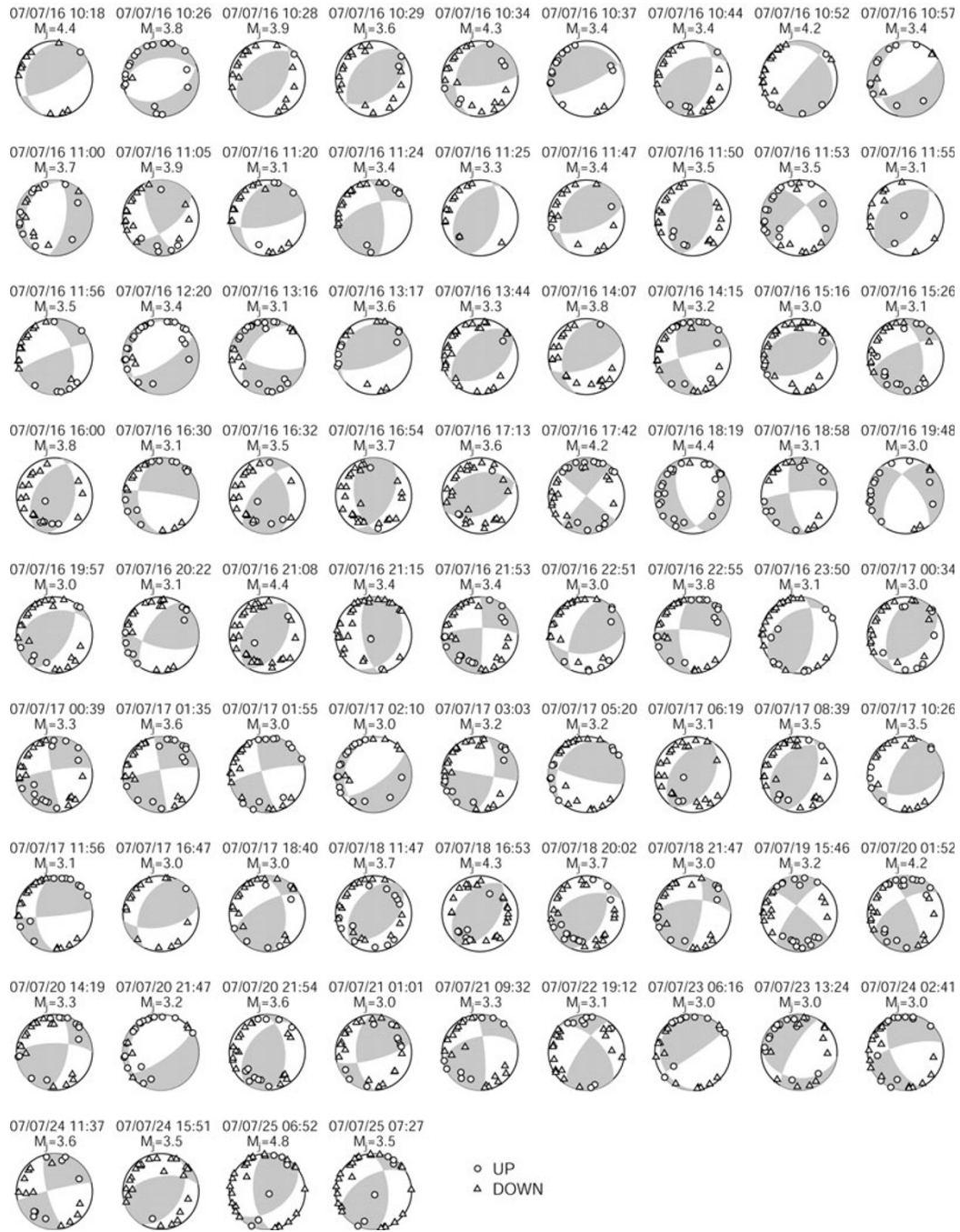
Fig. 5. Focal mechanism solutions of all events determined in our study (lower hemisphere of equal-area projection). Circles and triangles denote compressional and dilatational first motions, respectively. Origin time (JST) and magnitude are shown above each beach ball.

the aftershock region into five areas based on earthquake locations (Fig. 7). Most of the aftershocks for areas 1, 2, and 3 occurred at a depth range of 10–13 km, while ones deeper than 13 km occurred in areas 4 and 5. In the inversion, we omitted three events whose locations are far from all areas. Six normal fault events (mostly occurring in area 2) were also excluded because they made the inversion unstable. We believe that these normal fault events were triggered by a local heterogeneous stress field due to the mainshock rupture.

In order to be able to apply Michael's inversion method to focal mechanism solutions, we need to distinguish between the fault and the auxiliary plane. For small earthquakes, however, it is difficult to choose one plane from each fo-

cal mechanism as the actual fault plane. This problem is accounted for in the bootstrap resampling technique to calculate confidence regions for the stress tensor by assuming that a certain percentage of the planes are picked incorrectly (Michael, 1987). In the present study, we assumed for the bootstrap that each nodal plane had the same probability of being chosen during the resampling. Based on this assumption, we used 2000 bootstrap samples to obtain the 95% confidence region, which is adequate to produce stable confidence regions up to the 95% level (Michael, 1987). The results of the stress tensor inversion are shown in Fig. 7. The 95% confidence regions of the stress orientations are relatively large because of the small number of mechanisms
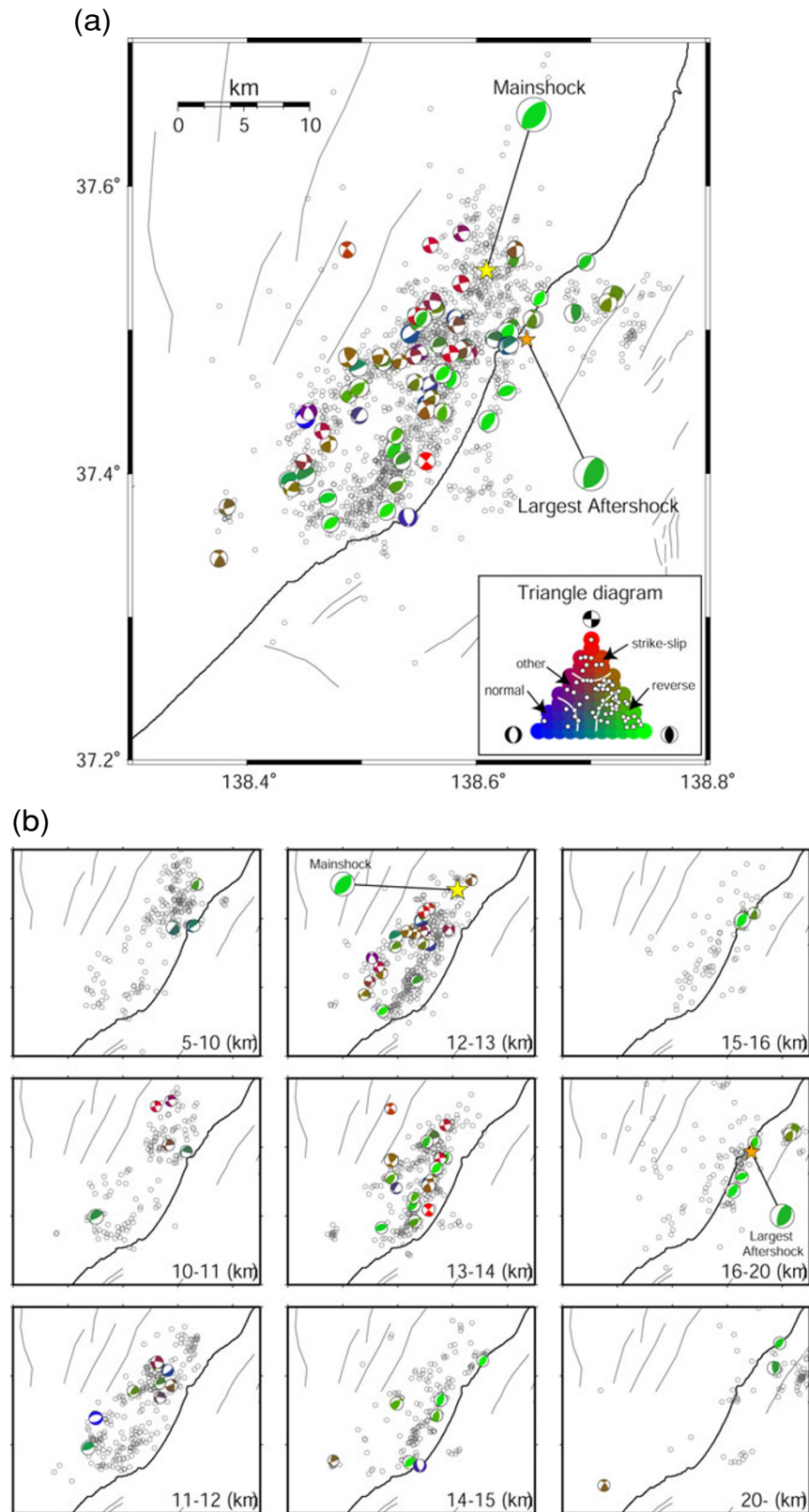
(a)

(b)

Fig. 6. Spatial distribution of focal mechanism solutions (lower hemisphere of equal-area projection), where different colors are used to differentiate reverse (green), strike-slip (red), and normal (blue) faulting mechanisms. A triangle diagram (Flohlich, 1992) with a color scale is shown in the lower right inset. (a) All focal mechanisms. (b) Focal mechanisms in nine different depth ranges.

available. Despite these large 95% confidence regions, the stress tensor inversion reveals a clear spatial variation of the stress field on a scale that is smaller than the mainshock fault dimension. The stress orientation and confidence re-

gions in area 1 indicate a strike-slip faulting regime with a stress ratio of $\phi = 0.29$. The maximum principal stress S_1 is subhorizontal and trends N132°E. For area 2, the 95% confidence regions of S_2 and S_3 form a girdle, suggesting a
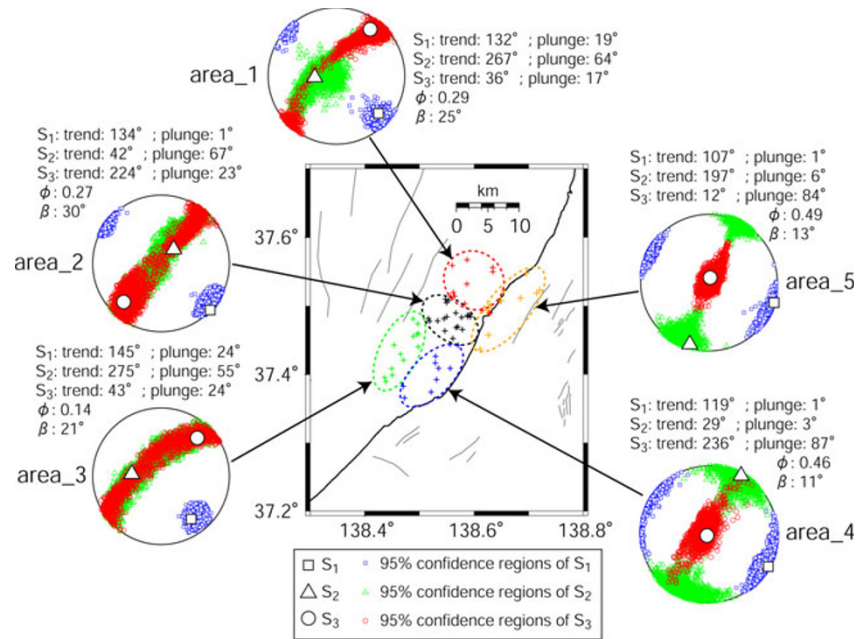
Fig. 7. Map of the stress tensor inversion results. Principal stress axes with their 95% confidence regions are plotted on lower hemisphere stereonets.

mixture of reverse and strike-slip faulting regime. We were able to clearly differentiate the maximum principal stress S_1 from S_2 and S_3, trending N134°E subhorizontally. The stress field in area 3 can be seen to be similar to that in area 2, except for the stress ratio ϕ. The stress fields in areas 4 and 5 are almost same, where stress orientation and confidence regions indicate a reverse faulting regime. The stress ratio ϕ is about 0.5 for both areas, implying that the magnitude of S_2 is close to $(S_1 + S_3)/2$. Unfortunately, the azimuths of principal stresses for these two areas are poorly constrained due to large 95% confidence regions.

Lund and Townend (2007) demonstrated that the direction of maximum "horizontal" compressive stress ($S_{H\max}$) is not always equal to the trend of the larger of the two subhorizontal principal stresses. The difference depends not only on the plunges of the principal stress axes but also on the stress ratio ϕ. Following the method of Lund and Townend (2007), we computed the true axis of $S_{H\max}$ from the four stress parameters determined by the stress tensor inversion (the directions of the three principal stresses and the stress ratio ϕ). Figure 8 shows the frequency of $S_{H\max}$ computed from the stress parameters that are within the 95% confidence regions. Here, 180° is subtracted from azimuth, if necessary, to ensure that all orientations plot in the range from 0° to 180°. The range of $S_{H\max}$ within the 95% confidence regions is generally consistent with that of the regional one (e.g., Townend and Zoback, 2006). It would appear that the $S_{H\max}$ direction on the western side of the source region (areas 1 and 3) is different from that on the eastern side (areas 4 and 5). However, we cannot exclude the possibility of a uniform $S_{H\max}$ direction across the entire region because the 95% confidence regions of $S_{H\max}$ overlap each other.
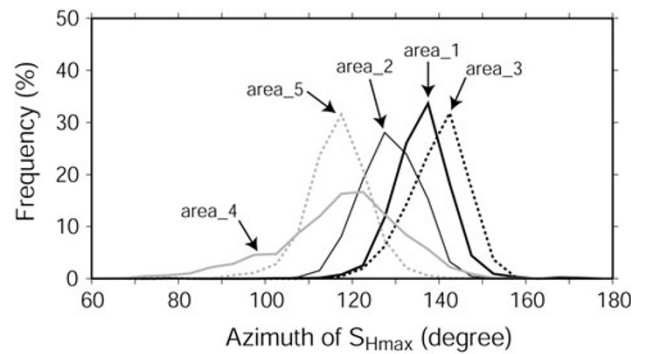

Fig. 8. The frequency of the true axis of $S_{H\max}$ computed from the 95% confidence regions of the stress tensor inversion results.

6.   Inference of the Pre-Mainshock Stress Field

The stress field determined in our study represents the post-mainshock stress field because aftershock focal mechanisms were used. Using a similar approach, we can estimate the pre-mainshock stress field from focal mechanism solutions of prior earthquakes that occurred in the aftershock area (e.g., Hauksson, 1994). For the 2007 Niigataken Chuetsu-oki earthquake, however, most of the prior seismicity does not overlap with aftershock distributions (Fig. 3). Furthermore, it is difficult to obtain reliable focal mechanisms of prior earthquakes because most of the prior events had a magnitude of less than 2. Thus, we cannot obtain the pre-shock stress field from focal mechanism solutions of prior earthquakes. Instead, we inferred the pre-shock stress field by comparing the stress field estimated in our study with the theoretical post-shock stress field computed by combining the stress change due to the mainshock and assumed pre-shock stresses. A similar approach was used by Oppenheimer et al. (1988) to study the 1984 M_L 6.2 Morgan Hill earthquake. In order to avoid confusion with
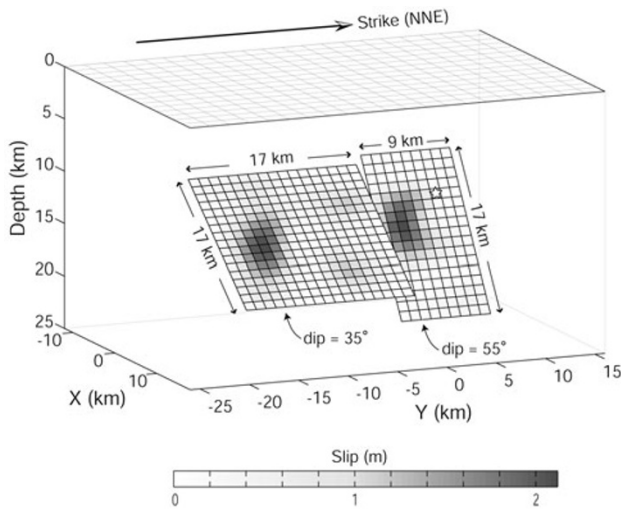
Fig. 9.   A finite fault slip model of Horikawa (2008) for the 2007 Niigataken Chuetsu-oki earthquake. The Y-axis corresponds to the strike of the earthquake. The hypocenter of the mainshock is located at a depth of 12.5 km (star).

symbols used in the previous section, we define σ_1, σ_2, and σ_3 as the pre-mainshock maximum, intermediate, and minimum compressive principal stress, respectively.

To calculate the stress change due to the mainshock, we used a finite fault source model of Horikawa (2008) derived from the inversion of near-source ground motions, which is generally consistent with those obtained in other studies (e.g., Aoi *et al*., 2008; Cirella *et al*., 2008; Ozawa, 2008). Horikawa's source model comprises two southeast dipping faults having different dimensions and dip angles (Fig. 9). The slip distribution inverted along a fixed 90° rake direction is characterized by two principal asperities and some minor ones, and total seismic moment is 6.54×10^{18} N m ($M_w = 6.5$). Using this slip model, we computed the stress change associated with the earthquake in an elastic half-space (Okada, 1992) under the assumption of a shear modulus of 32 GPa and a Poisson's ratio of 0.25.

For the pre-mainshock stress field, we assumed the orientation of σ_1 is horizontal and perpendicular to the strike of the mainshock fault (X-axis in Fig. 9). This assumption is consistent with extensive geologic (Yanagisawa *et al*., 1985; Sato, 1994), geodetic (Sagiya *et al*., 2000; Mazzotti *et al*., 2001), and seismic observations (Townend and Zoback, 2006) made in the northeast Japan, which could explain the presence and co-evolution of extensive compressional features such as folds and reverse faults. We considered it also reasonable to assume that the orientation of σ_3 is vertical because the study area is generally characterized by a reverse faulting regime. Thus, σ_2 is oriented parallel to the strike of the mainshock fault. Since there no information was available on the magnitudes of the principal stresses, we tried to constrain these by comparing the stress fields obtained by the stress tensor inversion (Fig. 7) with a theoretically calculated stress field.

We first investigated the stress field around areas 1, 2, and 3. Figure 10 shows a number of examples of predicted post-mainshock stress fields which were averaged over the depth range of 10–13 km with a depth increment of 1 km. The fi-

nal stress field is indicated by lower hemisphere, equal-area "beach-balls" plotted at 2-km spacing, where the direction of σ_1 lies in the center of the unshaded quadrant. The same color triangle diagram as that in Fig. 6 is used to differentiate stress fields. Figure 10 suggests that the difference in the magnitude of σ_2 and σ_3 must be less than a few MPa to produce a strike-slip faulting regime. Here, the distribution of the strike-slip faulting regime is consistent with the locations of asperities. When the difference in the magnitude of σ_2 and σ_3 is larger than about 5 MPa, a reverse faulting regime always dominates the post-shock stress field, which is inconsistent with our observational result (Fig. 7). Taking the spatial distribution of the strike-slip faulting regime into consideration, we infer that the difference in the magnitude of σ_2 and σ_3 is 2 MPa. We also found that the differential stress ($\sigma_1 - \sigma_3$) needs to exceed at least 10 MPa because in the case of a smaller differential stress, the direction of maximum principal stress significantly scatters, and a normal faulting stress field appears in some areas. Thus, the following stress state could be a plausible pre-shock one for the areas 1, 2, and 3; σ_1 is dominant, and the difference in σ_2 and σ_3 is small (2 MPa). In this paper, we call this stress state the "uniaxial" stress state. Based on the observation that the concentrated WNW-ESE contraction is occurring in this region (Sagiya *et al*., 2000; Mazzotti *et al*., 2001), the uniaxial stress state is reasonable.

If the same uniaxial stress state prevails across the entire region, the stress field in the areas 4 and 5 also becomes a strike-slip faulting regime or a mixture of a strike-slip and reverse faulting regime. However, this situation is inconsistent with our observational result that a reverse-faulting regime dominates the post-shock stress fields here. We found that the computed post-shock stress field approaches agreement with the observation when the difference in the magnitude of σ_2 and σ_3 is increased by at least a few MPa. Unfortunately, the combined uncertainties in the slip model and the result of stress tensor inversion make it difficult to conclude that the pre-shock stress field in areas 4 and 5 was different from that in areas 1, 2, and 3.

As already mentioned, a northwest dipping fault may exist near the hypocenter of the mainshock (Kato *et al*., 2008; Yukutake *et al*., 2008). Therefore, we investigated how the post-mainshock stress field changes when we add a northwest-dipping fault to Horikawa's fault model as shown in Fig. 11(a). Here, the value of the static stress drop along the northwest-dipping fault plane is assumed to be 10 MPa, resulting in an average slip of about 84 cm. Figure 11(b) shows a number of examples of predicted post-mainshock stress fields, in which the pre-mainshock stress fields are consistent with those in the middle panel of Fig. 10. The only difference in the post-mainshock stress fields between the two models is that the spatial distribution of the strike-slip faulting regime in the northern area becomes slightly larger when the northwest dipping fault exists. As the difference is not significant at a spatial scale of a few kilometers, we conclude that the addition of the northwest-dipping fault does not alter our conclusions. In other words, this result suggests that the results of our analysis alone cannot distinguish which model explains the observation better.
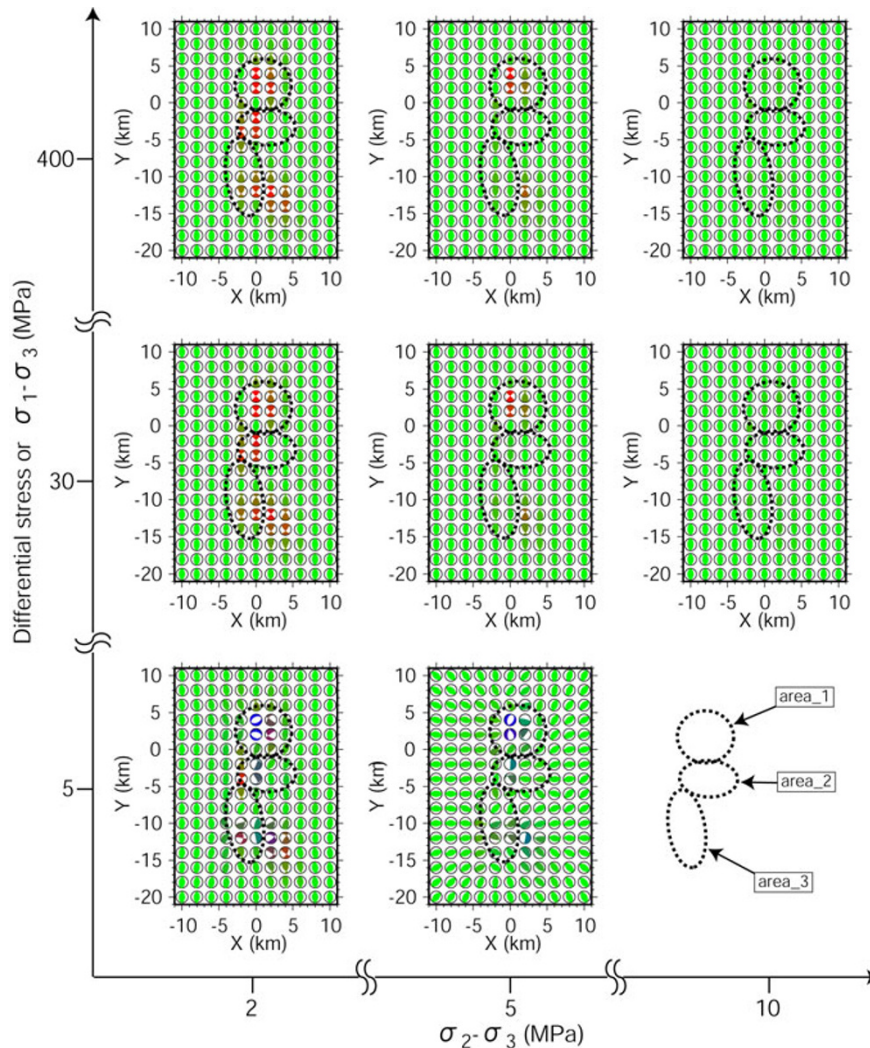
Fig. 10. Predicted post-mainshock stress fields for areas 1, 2, and 3 using Horikawa's (2008) slip model in combination with different pre-shock stress fields. These three areas are defined in Fig. 7 and are shown by dotted ellipses in this figure. The final stress field is indicated by lower hemisphere, equal-area "beach-balls" plotted at 2-km spacing, where the direction of σ_1 lies at the center of the unshaded quadrant. The same color triangle diagram as that in Fig. 6(a) is used to differentiate stress fields.

7. Discussion

There are many observations that the stress release associated with large and moderate earthquakes perturbed the stress field in the source region. By inverting suites of focal mechanism solutions before and after the mainshock to infer the orientations of the principal stresses, many authors have been able to determine the temporal change in the maximum compressional stress axis (e.g., Hauksson, 1994; Zhao *et al.*, 1997; Provost and Houston, 2003; Ratchkovski *et al.*, 2004). For example, Hardebeck and Hauksson (2001) reported that the maximum compressional stress orientation rotated by 15° (±10°) after the 1992 $M_{\rm w}$ 7.3 Landers earthquake. For the 1999 $M_{\rm w}$ 7.6 Izmit earthquake, Polat *et al.* (2002) found that the stress field changed from a strike-slip faulting to a mixed strike-slip and normal faulting one. Temporal changes in the stress field are also suggested for other earthquakes, such as the 2002 $M_{\rm w}$ 7.9 Denali fault earthquake (Ratchkovski *et al.*, 2004) and the 2003 $M_{\rm w}$ 7.9 Tokachi Oki earthquake (Ghimire *et al.*, 2005). In northeast Japan, including the area of our study, the stress field is well known to be generally characterized by a reverse faulting

regime (Sato, 1994; Townend and Zoback, 2006). In contrast, we have shown that the stress field in area 1 is dominated by a strike-slip faulting regime and that areas 2 and 3 are characterized by a mixture of the strike-slip and reverse faulting regime, all of which are different from the regional faulting regime. By comparing the post-shock stress field estimated by the stress tensor inversion with the theoretically calculated one, we revealed that the stress changes associated with the 2007 Niigataken Chuetsu-oki earthquake, when added to the pre-shock uniaxial reverse-faulting stress field, could produce a strike-slip faulting regime in specific parts of the source region. Under this stress state, on the other hand, the σ_1 directions could not be significantly changed before and after the mainshock (Fig. 10). If the $S_{H\max}$ directions shown in Fig. 8 indicate spatial variation, they would have to originate in the spatial variation in the pre-shock $S_{H\max}$ directions—not in the temporal change.

Observations of temporal stress change stimulate our interest to make an attempt at inferring the level of stress at seismogenic depths, which would be a step towards a better understanding of large earthquake occurrence. By combin-
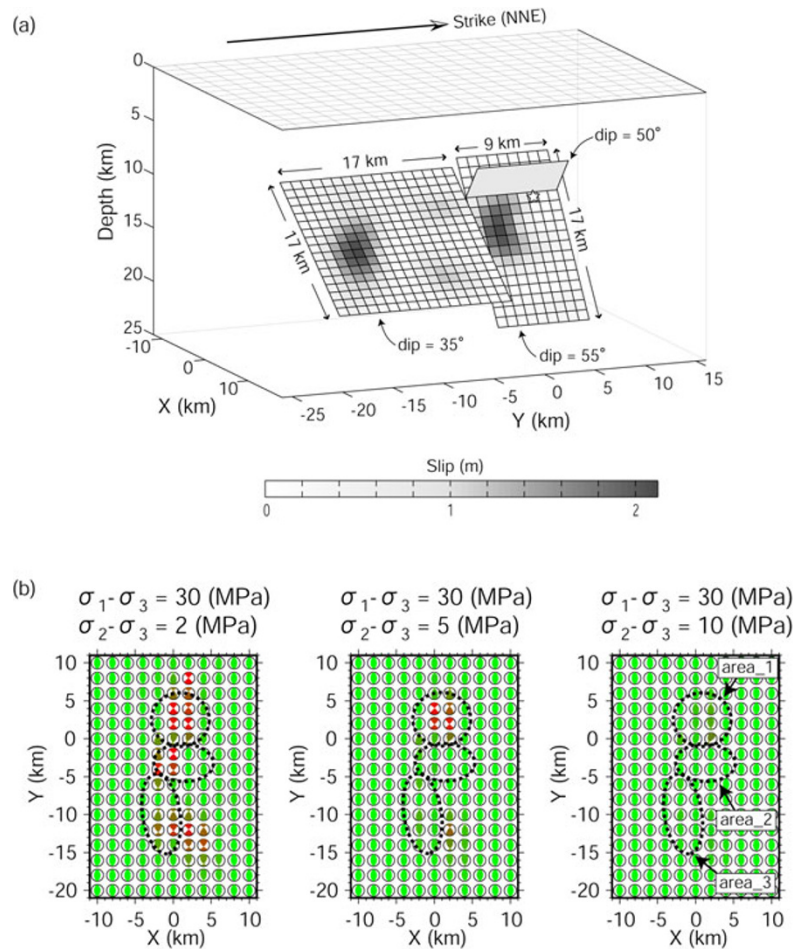
Fig. 11. (a) A Horikawa's fault model with a northwest dipping fault. The average slip on the northwest dipping fault is assumed to be about 84 cm. (b) Predicted post-mainshock stress fields based on a fault model shown in (a). Here, the pre-shock stress fields are consistent with those in the middle panel of Fig. 10.

ing the focal mechanisms of aftershocks and/or background seismicity with the stress change caused by the mainshock, a number of researchers have succeeded in constraining the pre-shock absolute stress at seismogenic depths (e.g., Kilb *et al.*, 1997; Hardebeck and Hauksson, 2001; Provost and Houston, 2003; Wesson and Boyd, 2007). Based on the results of these respective studies, the authors generally conclude that the differential stresses at seismogenic depths are the same as or smaller than the static stress changes generated by the mainshock, which are much smaller than those measured in boreholes. For the 2000 M_w 6.6 Western Tottori earthquake, Yukutake *et al.* (2007) found that the pre-shock differential stress at some areas seemed to be consistent with that estimated from borehole measurements. In our study, we inferred that the differential stress in the source region of the 2007 Niigataken Chuetsu-oki earthquake exceeded at least 10 MPa.

Townend and Zoback (2001) showed that there was little systematic difference in the pre- and post-earthquake stress orientations in the areas where pronounced activity occurred both before and after the 1992 M_w 7.3 Landers earthquake. Therefore, Townend (2006) suggests that in some cases the temporal changes in the stress field reported previously are in actual fact artifacts and that they simply reflect the spatial variations in stress imaged at different epochs by earthquakes occurring at different locations. In our study, however, this is not the case because we adopted a different approach that uses the aftershock focal mechanisms and the mainshock slip distribution. We assumed a uniform pre-mainshock stress field for the sake of simplification, but one may suggest that the temporal stress changes caused by past repeated earthquakes of this type remain in the source region, producing spatial variations in the pre-shock stress field. If the stress changes due to repeated earthquakes are simply added, however, the distribution of strike-slip faulting regime becomes significantly large, and the $S_{H\max}$ directions significantly deviate from the regional one (WNW-ESE direction). Therefore we infer that the strike-slip faulting regime caused by the mainshock will come close to returning to the regional one due to a kind of stress diffusion (e.g., Lehner *et al.*, 1981) during each earthquake cycle. Although the combined uncertainties in the slip model and the result of stress tensor inversion make it difficult to completely rule out a possibility of spatial variation in the pre-shock stress field, we believe that the temporal stress change due to the mainshock is the simplest scenario that explains the stress fields deduced from aftershock focal mechanisms.

8.   Conclusion

We relocated the hypocenters of the aftershocks of the 2007 Niigataken Chuetsu-oki earthquake and the prior seismicity based on appropriate velocity structures. We show that most of prior seismicity occurred outside the aftershock area and that it does not overlap with aftershock distributions. Focal mechanisms of aftershocks were then determined using P-wave polarity data as well as body wave amplitudes. We successfully obtained 76 aftershock focal mechanisms, which enabled us discuss the stress field in the source region after the mainshock. In addition to reverse faulting aftershocks that were similar to the mainshock, many aftershocks with large strike-slip components and a number of normal faulting aftershocks occurred across the entire region. A stress tensor inversion method revealed that the stress field in the source region spatially varied on a scale smaller than the fault dimension of the mainshock and that the stress field became a mixture of the strike-slip and reverse faulting regimes. In order to infer the pre-mainshock stress field, we compared the post-mainshock stress field estimated by the stress tensor inversion with the theoretical stress field that was computed using an observed non-uniform slip distribution of the mainshock and variously assumed pre-shock stress fields. The comparison suggests that the pre-mainshock principal stress in the WNW-ESE direction was dominant and that the magnitudes of the other two principal stresses were similar.

References

Aoi, S., H. Sekiguchi, N. Morikawa, and T. Kunugi, Source process of the 2007 Niigata-ken Chuetsu-oki earthquake derived from near-fault strong motion data, *Earth Planets Space*, **60**, 1131–1135, 2008.

Boatwright, J., Detailed spectral analysis of two small New York State earthquakes, *Bull. Seismol. Soc. Am.*, **68**, 1117–1131, 1978.

Cirella, A., A. Piatanesi, E. Tinti, and M. Cocco, Rupture process of the 2007 Niigata-ken Chuetsu-oki earthquake by non-linear joint inversion of strong motion and GPS data, *Geophys. Res. Lett.*, **35**, L16306, doi:10.1029/2008GL034756, 2008.

Flohlich, C., Triangle diagrams: ternary graphs to display similarity and diversity of earthquake focal mechanism, *Phys. Earth Planet. Inter.*, **75**, 193–198, 1992.

Geological Survey of Japan, AIST, Gravity CD-ROM of Japan, Ver. 2., Digital Geoscience Map P-2, 2004.

Ghimire, S., K. Katsumata, and M. Kasahara, Temporal changes in state of stress in the Tokachi Oki area after the 2003 Tokachi Oki Earthquake, *Earth Planets Space*, **57**, 83–91, 2005.

Hardebeck, J. L. and E. Hauksson, Crustal stress field in southern California and its implications for fault mechanics, *J. Geophys. Res.*, **106**(B10), 21,859–21,882, 2001.

Hashimoto, M., Horizontal strain rates in the Japanese Islands during interseismic period deduced from geodetic surveys (Part I): Honshu, Shikoku and Kyushu, *Zisin*, **43**, 13–26, 1990 (in Japanese with English abstract).

Hauksson, E., State of stress from focal mechanisms before and after the 1992 Landers earthquake sequence, *Bull. Seismol. Soc. Am.*, **84**, 917–934, 1994.

Hauksson, E., L. M. Jones, and K. Hutton, The 1994 Northridge earthquake sequence in California: Seismological and tectonic aspects, *J. Geophys. Res.*, **100**(B7), 12,335–12,355, 1995.

Hirata, N. and M. Matsu'ura, Maximum-likelihood estimation of hypocenter with origin time eliminated using nonlinear inversion technique, *Phys. Earth Planet. Inter.*, **47**, 50–61, 1987.

Horikawa, H., The 2007 Chuetsu-oki, Japan, Earthquake: Rupture over a complicated fault system, *Japan Geoscience Union Meeting*, S142-P002, 2008.

Imanishi, K., I. Cho, Y. Kuwahara, N. Hirata, and Y. Panayotopoulos, Focal mechanism solutions of microearthquakes around the southern part of the Itoigawa-Shizuoka Tectonic Line active fault system, *Annual Report on Active Fault and Paleoearthquake Researches*, No. 6, 55–70, 2006a (in Japanese with English abstract).

Imanishi, K., Y. Kuwahara, and Y. Haryu, Off-fault aftershocks of the 2005 West Off Fukuoka Prefecture Earthquake: Reactivation of a structural boundary?, *Earth Planets Space*, **58**, 81–86, 2006b.

Imanishi, K., Y. Kuwahara, T. Takeda, and Y. Haryu, The seismicity, fault structures, and stress field in the seismic gap adjacent to the 2004 Mid-Niigata earthquake inferred from seismological observations, *Earth Planets Space*, **58**, 831–841, 2006c.

Kato, A., S. Sakai, N. Hirata, E. Kurashimo, T. Iidaka, T. Iwasaki, and T. Kanazawa, Imaging the seismic structure and stress field in the source region of the 2004 mid-Niigata prefecture earthquake: Structural zones of weakness and seismogenic stress concentration by ductile flow, *J. Geophys. Res.*, **111**, B08308, doi:10.1029/2005JB004016, 2006.

Kato, A., S. Sakai, E. Kurashimo, T. Igarashi, T. Iidaka, N. Hirata, T. Iwasaki, T. Kanazawa, and Group for the aftershock observations of the 2007 Niigataken Chuetsu-oki Earthquake, Imaging heterogeneous velocity structures and complex aftershock distributions in the source region of the 2007 Niigataken Chuetsu-oki Earthquake by a dense seismic observation, *Earth Planets Space*, **60**, 1111–1116, 2008.

Kilb, D., M. Ellis, J. Gomberg, and S. Davis, On the origin of diverse aftershock mechanisms following the 1989 Loma Prieta earthquake, *Geophys. J. Int.*, **128**, 557–570, 1997.

Lehner, F. K., V. C. Li, and J. R. Rice, Stress diffusion along rupturing plate boundaries, *J. Geophys. Res.*, **86**(B7), 6155–6169, 1981.

Lund, B. and J. Townend, Calculating horizontal stress orientations with full or partial knowledge of the tectonic stress tensor, *Geophys. J. Int.*, doi:10.1111/j.1365–246X.2007.03468.x, 2007.

Mazzotti, S., P. Henry, and X. L. Pichon, Transient and permanent deformation of central Japan estimated by GPS, 2. Strain partitioning and arc-arc collision, *Earth Planet. Sci. Lett.*, **184**, 455–469, 2001.

Michael, A. J., Determination of stress from slip data: faults and folds, *J. Geophys. Res.*, **89**(B13), 11,517–11,526, 1984.

Michael, A. J., Use of focal mechanisms to determine stress: A control study, *J. Geophys. Res.*, **92**(B1), 357–368, 1987.

Okada, Y., Internal deformation due to shear and tensile faults in a half-space, *Bull. Seismol. Soc. Am.*, **82**, 1018–1040, 1992.

Okada, Y., K. Kasahara, S. Hori, K. Obara, S. Sekiguchi, H. Fujiwara, and A. Yamamoto, Recent progress of seismic observation networks in Japan—Hi-net, F-net, K-NET and KiK-net—, *Earth Planets Space*, **56**, xv–xxviii, 2004.

Oppenheimer, D. H., P. A. Reasenberg, and R. W. Simpson, Fault plane solutions for the 1984 Morgan Hill, California, earthquake sequence: Evidence for the state of stress on the Calaveras fault, *J. Geophys. Res.*, **93**(B8), 9007–9026, 1988.

Ozawa, T., Coseismic deformation of the 2007 Chuetsu-oki Earthquake derived from PALSAR/InSAR and its fault model, *Earth Planets Space*, **60**, 1099–1104, 2008.

Polat, O., H. Haessler, A. Cisternas, H. Philip, H. Eyidogan, M. Aktar, M. Frogneux, D. Comte, and C. Gürbüz, The Izmit (Kocaeli), Turkey Earthquake of 17 August 1999: Previous seismicity, aftershocks, and seismotectonics, *Bull. Seismol. Soc. Am.*, **92**, 361–375, 2002.

Provost, A.-S. and H. Houston, Investigation of variations in stress orientations before and after four major earthquakes in California, *Phy. Earth Planet. Inter.*, **139**, 255–267, 2003.

Ratchkovski, N. A., S. Wiemer, and R. A. Hansen, Seismotectonics of the central Denali fault, Alaska, and the 2002 Denali fault earthquake sequence, *Bull. Seismol. Soc. Am.*, **94**, S156–S174, 2004.

Research Group for Active Faults of Japan, *Active Faults of Japan*, University of Tokyo Press, 1991 (in Japanese).

Sagiya, T., S. Miyazaki, and T. Tada, Continuous GPS array and present-day crustal deformation of Japan, *Pure Appl. Geophys.*, **157**, 2303–2322, 2000.

Sato, H., The relationship between late Cenozoic tectonic events and stress field and basin development in northeast Japan, *J. Geophys. Res.*, **99**(B11), 22,261–22,274, 1994.

Shinohara, M., T. Kanazawa, T. Yamada, K. Nakahigashi, S. Sakai, R. Hino, Y. Murai, A. Yamazaki, K. Obana, Y. Ito, K. Iwakiri, R. Miura, Y. Machida, K. Mochizuki, K. Uehira, M. Tahara, A. Kuwano, S. Amamiya, S. Kodaira, T. Takanami, Y. Kaneda, and T. Iwasaki, Precise aftershock distribution of the 2007 Chuetsu-oki Earthquake obtained by using an ocean bottom seismometer network, *Earth Planets Space*, **60**, 1121–1126, 2008.

Sibson, R. H., An episode of fault-valve behavior during compressional inversion?—The 2004 M_J 6.8 Mid-Niigata Prefecture, Japan, earthquake sequence, *Earth Planet. Sci. Lett.*, **257**, 188–199, 2007.

Takeda, T., H. Sato, T. Iwasaki, N. Matsuda, S. Sakai, T, Iidaka, and A. Kato, Crustal structure in the northern Fossa Magna region, central Japan, modeled from refraction/wide-angle reflection data, *Earth Planets Space*, **56**, 1293–1299, 2004.

Townend, J., What do faults feel? Observational constraints on the stresses acting on seismogenic faults, in *Earthquakes: Radiated energy and the physics of faulting*, edited by Abercrombie *et al.*, AGU Geophysical Monograph Series, **170**, 313–327, 2006.

Townend, J. and M. D. Zoback, Implications of earthquake focal mechanisms for the frictional strength of the San Andreas fault system, in *The Nature and Significance of Fault Zone Weakening*, edited by R. E. Holdsworth *et al.*, **186**, 13–21, Geological Society of London Special Publication, 2001.

Townend, J. and M. D. Zoback, Stress, strain, and mountain building in central Japan, *J. Geophys. Res.*, **111**, B03411, doi:10.1029/2005JB003759, 2006.

Waldhauser, F. and W. L. Ellsworth, A double-difference earthquake location algorithm: Method and application to the Northern Hayward fault, California, *Bull. Seismol. Soc. Am.*, **90**, 1353–1368, 2000.

Wessel, P. and W. H. F. Smith, New, improved version of the Generic Mapping Tools released, *Eos Trans. AGU*, **79**, 579, 1998.

Wesson, R. L. and O. S. Boyd, Stress before and after the 2002 Denali fault earthquake, *Geophys. Res. Lett.*, **34**, L07303, doi:10.1029/2007GL029189, 2007.

Yanagisawa, Y., K. Chihara, I. Suzuki, T. Uemura, K. Kodama, and H. Kato, Geology of the Tokamachi district, with geological sheet map at 1:50,000, 104 pp., Geol. Surv. Jpn., Tokyo, 1985 (in Japanese with English abstract).

Yukutake, Y., Y. Iio, H. Katao, and T. Shibutani, Estimation of the stress field in the region of the 2000 Western Tottori Earthquake: Using numerous aftershock focal mechanisms, *J. Geophys. Res.*, **112**, B09306, doi:10.1029/2005JB004250, 2007.

Yukutake, Y., T. Takeda, and K. Obara, Well-resolved hypocenter distribution using the double-difference relocation method in the region of the 2007 Chuetsu-oki earthquake, *Earth Planets Space*, **60**, 1105–1109, 2008.

Zhang, H. and C. H. Thurber, Double-difference tomography: The method and its application to the Hayward fault, California, *Bull. Seismol. Soc. Am.*, **93**, 1875–1889, 2003.

Zhao, D., H. Kanamori, and D. Wiens, State of stress before and after the 1994 Northridge earthquake, *Geophys. Res. Lett.*, **24**(5), 519–522, 1997.

Zoback, M. D. and G. C. Beroza, Evidence for near-frictionless faulting in the 1989 (M6.9) Loma Prieta, California, earthquake and its aftershocks, *Geology*, **21**, 181–185, 1993.

K. Imanishi (e-mail: imani@ni.aist.go.jp) and Y. Kuwahara